Smart Structures and Systems, *Vol. 25, No. 5 (2020) 531-541*
DOI: https://doi.org/10.12989/sss.2020.25.5.531

Post-earthquake building safety evaluation using consumer-grade surveillance cameras

Ting Y. Hsu*[1,2], Quang V. Pham [2a], Wei C. Chao [3c] and Yuan S. Yang [3c]

[1] *Department of Civil and Construction Engineering, National Taiwan University of Science and Technology, Taipei 10607, Taiwan*
[2] *Taiwan Building Technology Center, National Taiwan University of Science and Technology, Taipei 10607, Taiwan*
[3] *Taiwan Department of Civil Engineering, National Taipei University of Technology, Taipei 10608, Taiwan*

(*Received May 28 2019, Revised December 26, 2019, Accepted December 27, 2019*)

Abstract. This paper demonstrates the possibility of evaluating the safety of a building right after an earthquake using consumer-grade surveillance cameras installed in the building. Two cameras are used in each story to extract the time history of interstory drift during the earthquake based on camera calibration, stereo triangulation, and image template matching techniques. The interstory drift of several markers on the rigid floor are used to estimate the motion of the geometric center using the least square approach, then the horizontal interstory drift of any location on the floor can be estimated. A shaking table collapse test of a steel building was conducted to verify the proposed approach. The results indicate that the accuracy of the interstory drift measured by the cameras is high enough to estimate the damage state of the building based on the fragility curve of the interstory drift ratio. On the other hand, the interstory drift measured by an accelerometer tends to underestimate the damage state when residual interstory drift occurs because the low frequency content of the displacement signal is eliminated when high-pass filtering is employed for baseline correction.

Keywords: consumer-grade surveillance cameras; post-earthquake building safety evaluation; interstory drift

1. Introduction

Aftershocks often take place after an earthquake, and these aftershocks can cause extensive damage to buildings (Yazgan and Dazio 2012). For this reason, a post-earthquake evaluation of building structure should be conducted as quickly as possible to help experts assess a building's safety. Not only does a speedy and reliable post-earthquake damage evaluation prevent people from returning unsafe buildings, it also brings enormous social and economic benefits by diminishing the amount of time during which normal activities are disrupted. For instance, when a high-tech factory experiences a large earthquake, structural safety should be guaranteed before technicians can be sent back into the factory to rescue valuable equipment and products. With a post-earthquake damage assessment system, the time for ensuring structural integrity could be greatly shortened.

Interstory drift is a valuable metric that can be used to immediately estimate the damaged status of an existing building structure after an earthquake. Naeim *et al*. (2006) examined the application of different approaches for immediate post-earthquake damage assessments in a study involving more than 40 instrumented buildings that was conducted under the California Strong Motion Instrumentation Program. The study concluded that an approach to the post-earthquake damage assessment of buildings based on the estimated maximum interstory drift ratio (IDR) and the application of various fragility curves is highly effective. However, that study used accelerometers as the measurement sensors. The double integration of acceleration measurement was performed by means of numerical integration, and then a high-pass filter was often used to remove the low-frequency drift. Therefore, the low-frequency range of structural displacement estimated using the acceleration signals was inaccurate (Trapani *et al*. 2015, Park *et al*. 2013). As a result, there were certainly errors in the accuracy of the maximum interstory drift measurements when residual displacement did exist.

Currently, besides double integration from acceleration, there are several available approaches for measuring displacement, such as the linear variable differential transducer (LVDT), laser Doppler vibrometer (LDV), total station, and global positioning system (GPS) approaches. The LVDT and LDV approaches are highly accurate; however, the installation of LVDTs and LDVs requires additional supporting structures that reduce the interior space inside a building; hence, their application in the field is limited (Lee *et al*. 2017). Moreover, although the GPS and total station methods can be used to measure the static and dynamic displacement of a building structure, multipath effects and their low sampling frequencies have a significant influence on the accuracy of these methods for

*Corresponding author, Associate Professor,
E-mail: tyhsu@mail.ntust.edu.tw
[a] Master Student, E-mail: quangvinhphamhau@gmail.com
[b] Master Student, E-mail: a0981076023@gmail.com
[c] Ph.D., Associate Professor, E-mail: ysyang@ntut.edu.tw

http://www.techno-press.org/?journal=sss&subpage=7
ISSN: 1738-1584 (Print), 1738-1991 (Online)

dynamic displacement measurements. Skolnik and Wallace (2010) also summarize the state-of-the-art and potential future methodologies for measuring interstory drift, and then conclude that accurate and reliable measurement of interstory drift remains a significant technical challenge.

Over the past decade, the rapid development of vision technology and computer science have opened opportunities for measuring lateral displacement using vision-based measurement systems (Yoon *et al*. 2016, Khuc and Catbas 2017). A vision-based measurement system normally consists of digital cameras and a computer system, with computational software analyzing and tracking the movement of target points in videos recorded by the cameras. Vision-based measurement approaches have a number of valuable advantages, such as low instrument cost, ease of setup and operation, and flexibility in extracting the displacement of any points on the structure from the video measurements. Moreover, Harvey and Elisha (2018) performed a shaking table test to illustrate the feasibility of extracting the fundamental period of a building using the cameras installed inside the building. Instrumentation costs can be eliminated if existing cameras inside a building are leveraged for response measurements.

As pointed out above, vision-based displacement measurement approaches have many advantages and are capable of capturing accurate structural vibration signals for system identification and damage detection. However, the application of vision-based displacement measurements (made using consumer-grade cameras installed inside buildings) to assess building damage states has not been well-studied. In this study, vision-based displacement measurements were achieved by using typical consumer-grade surveillance cameras, and the methodology is introduced in the next section. Shaking table experiments involving a steel building affected by different levels of seismic excitations are then introduced in the third section. The results are discussed in the fourth section, and the conclusions are presented in the final section.

2. Methodology

2.1 Vision-based displacement measurement

This study used a vision-based approach to monitor the interstory drift between the cameras on the ceiling and the markers on the floor. An image analysis software toolbox called ImPro Stereo was previously developed to measure displacement and strain fields (Yang *et al*. 2012, 2015, 2018). This study employed the ImPro Stereo toolbox to translate the markers' positions from 2-D image coordinates in pixel units to 3-D physical coordinates in engineering units. The ImPro Stereo toolbox uses the camera calibration, stereo triangulation, and image template matching techniques to track the response vibration of the points of interest of an object and then obtain their displacement time-history data. This method computes the markers' positions in 3D coordinates by using images taken from two cameras. For displacement measurements, it is common to use a rectangular corner with high contrast as a marker, and the marker used in this study was a four-cell chess-pattern board.

Fig. 1 The chess-pattern board used for camera calibration

An 11-by-8 chess-pattern board was used for camera calibration, as shown in Fig. 1. Two cameras concurrently took several pairs of calibration photos as the position of the chessboard was changed. These calibration images were then analyzed to estimate intrinsic and extrinsic parameters. Next, the calibration results and sequential images taken during an earthquake excitation by the two cameras were imported into the ImPro Stereo toolbox. Most of the computer implementation of the ImPro Stereo toolbox was built upon MATLAB codes with an external call to a C/C++ based OpenCV library. Camera calibration can be done by running a camera calibration tool with the input of calibration photos and the real size of the chessboard cell. This study used Bouguest's toolbox (Bouguet 2014) because it can provide all the necessary parameters to run the ImPro Stereo toolbox. The camera calibration results include extrinsic parameters and intrinsic parameters. The extrinsic parameters between two cameras consist of the rotational matrix $\boldsymbol{R}$ and the translational vector $\boldsymbol{T}$. The intrinsic parameters of each camera consist of the focal lengths f_x and f_y, the skew factor α, the principal points c_x and c_y, and the distortion factors k_1, k_2, k_3, k_4, and k_5.

The basic formulations of the camera calibration are introduced as follows. A point $\boldsymbol{P}$ in the world coordinate $\boldsymbol{X_W}$ is expressed as (Bouguet 2014)

$$\boldsymbol{X_W} = [x_W, y_W, z_W]^T \tag{1}$$

A point $\boldsymbol{P}$ in a camera coordinate $\boldsymbol{X_C}$ is expressed as

$$\boldsymbol{X_C} = [x_C, y_C, z_C]^T = \boldsymbol{R_C} \times \boldsymbol{X_W} + \boldsymbol{T_C} \tag{2}$$

Where $\boldsymbol{R_C}$ and $\boldsymbol{T_C}$ describe the relative position and the view angle of the camera, respectively.

Then, $\boldsymbol{X_C}$ is projected to the z = 1 plane in the camera coordinate system to generate the normalized coordinate $\boldsymbol{X_N}$

$$\boldsymbol{X_N} = [x_N, y_N]^T = \left[\frac{x_C}{z_C}, \frac{y_C}{z_C}\right]^T \tag{3}$$

The relationship between the normalized coordinate system and the image coordinate system is nonlinear. It can be expressed as

$$\boldsymbol{X_I} = \begin{bmatrix} f_x & \alpha \cdot f_x & c_x \\ 0 & f_y & c_y \end{bmatrix} \begin{bmatrix} (1 + k_1 r^2 + k_2 r^4 + k_5 r^6) x_N + 2k_3 x_N y_N + k_4 (r^2 + 2x_N^2) \\ (1 + k_1 r^2 + k_2 r^4 + k_5 r^6) y_N + 2k_4 x_N y_N + k_3 (r^2 + 2y_N^2) \\ 1 \end{bmatrix} \quad (4)$$

$$r = \sqrt{x_D^2 + y_D^2} \quad (5)$$

In brief, the camera calibration process solves a nonlinear optimization problem to find a set of parameters that satisfies the above equations from Eqs. (1) to (5). When the position of the grid corner (x_W, y_W, z_W) is known in the world coordinates, the position of the grid corner (x_I, y_I) in the image coordinates can be found automatically using Bouguest's toolbox. The extrinsic parameters $\boldsymbol{R}$ and $\boldsymbol{T}$ (i.e., the transformation between the two cameras' coordinate systems) are calculated from the $\boldsymbol{R_C}$ and $\boldsymbol{T_C}$ of each camera (i.e., the conversion between the camera coordinate system and the world coordinate system).

A sub-pixel based digital image correlation (DIC) method is utilized to obtain the location of the marker in an image. The DIC method is an intensive procedure based on template matching that has been implemented in OpenCV (Bradski and Kaehler 2008). This study employed a modified template matching method that obtains accurate sub-pixels by multi-level image resize procedures. The precision of the sub-pixel template matching in this study was set to 0.02 pixels.

Ideally, the position of the target point in 3D coordinates is the intersection of two rays. However, two rays may never intersect with each other due to various errors in the analysis process. For this reason, the intersection is defined as an optimized point that is closest to both rays. Stereo triangulation calculates the 3D position of a marker according to the image coordinates of the marker in two images taken by two cameras. The relationship between the location of the marker in the left-camera $\boldsymbol{X_L}$ and the location of the marker in the right-camera $\boldsymbol{X_R}$ can be expressed as (Bradski and Kaehler 2008)

$$\boldsymbol{X_R} = \boldsymbol{R}\boldsymbol{X_L} + \boldsymbol{T} \quad (6)$$

$\boldsymbol{X_L}$ and $\boldsymbol{X_R}$ can be determined as

$$\boldsymbol{X_L} \cong \alpha_L \boldsymbol{X_{NL}} \quad (7)$$

$$\boldsymbol{X_R} \cong \alpha_R \boldsymbol{X_{NR}} \quad (8)$$

Where $\boldsymbol{X_{NL}}$ and $\boldsymbol{X_{NR}}$ are the projected marker on the z = 1 plane in the left and right camera coordinates, respectively. These values can be determined from the inverse function of Eq. (4) by using iteration in the program. The intersection of two rays can be expressed as

$$\boldsymbol{X_L} = 0.5\left(\alpha_L \boldsymbol{X_{NL}} + \boldsymbol{R}^T(\alpha_R \boldsymbol{X_{NR}} - \boldsymbol{T})\right) \quad (9)$$

Where

$$\alpha_L = \frac{(\boldsymbol{RX_{NL}} \cdot \boldsymbol{X_{NR}})(\boldsymbol{X_{NR}} \cdot \boldsymbol{T}) - (\boldsymbol{X_{NR}} \cdot \boldsymbol{X_{NR}})(\boldsymbol{RX_{NL}} \cdot \boldsymbol{T})}{(\boldsymbol{X_{NL}} \cdot \boldsymbol{X_{NL}})(\boldsymbol{X_{NR}} \cdot \boldsymbol{X_{NR}}) - (\boldsymbol{RX_{NL}} \cdot \boldsymbol{X_{NR}})^2} \quad (10)$$

$$\alpha_R = \frac{(\boldsymbol{X_{NL}} \cdot \boldsymbol{X_{NL}})(\boldsymbol{X_{NR}} \cdot \boldsymbol{T}) - (\boldsymbol{RX_{NL}} \cdot \boldsymbol{T})(\boldsymbol{RX_{NL}} \cdot \boldsymbol{X_{NR}})}{(\boldsymbol{X_{NL}} \cdot \boldsymbol{X_{NL}})(\boldsymbol{X_{NR}} \cdot \boldsymbol{X_{NR}}) - (\boldsymbol{RX_{NL}} \cdot \boldsymbol{X_{NR}})^2} \quad (11)$$

Furthermore, error in stereo triangulation is unavoidable and should be taken into consideration in practical applications. The locations of the projected points in images $\boldsymbol{X_{NL}}$ and $\boldsymbol{X_{NR}}$ positively contain errors due to the limitation of image resolution and the effect of the noise. Moreover, when two cameras are roughly parallel with each other, the denominators in Eqs. (10) and (11) are characteristically small. Consequently, the error along the depth (that is, in the cameras' viewing directions) could be amplified. Assuming that the triangle of two cameras and the marker is an isosceles triangle, then the relationship between the error of depth err_D and the error in image err_I is close to

$$err_D \cong err_I \frac{D}{L} \quad (12)$$

Where the depth D is the estimated distance from the marker to the two cameras, and L is the length between the two cameras. Generally, the depth D is much greater than the distance between the two cameras. Correspondingly, the error of the depth is significantly larger than the error of the image. However, unlimitedly increasing the camera distance L is not a good idea for reducing the depth error, because when the gap between the two cameras is too large, the images from the two cameras become inconsistent.

If the locations of the mass center and the stiffness center of a floor in a building are not the same, the torsional motion of the floor during an earthquake should be considered. Since the floor deck was assumed to be a rigid body in this study, the relative motion of the geometric center of the floor could be estimated if the interstory drifts of more than two markers on the floor were traced during an earthquake. The relationship between the interstory drift of the markers, i.e., $\bar{X}_i$ and $\bar{Y}_i$, $i = 1,2,\ldots,n$, and the relative motion of the geometric center, i.e., $\bar{X}_c$, $\bar{Y}_c$, and $\bar{\theta}_c$ can be represented using the following equation

$$\begin{bmatrix} \bar{Y}_1 \\ \bar{Y}_2 \\ \vdots \\ \bar{Y}_n \\ \bar{X}_1 \\ \bar{X}_2 \\ \vdots \\ \bar{X}_n \end{bmatrix} = \begin{bmatrix} X_1 & 1 & 0 \\ X_2 & 1 & 0 \\ \vdots & \vdots & \vdots \\ X_n & 1 & 0 \\ Y_1 & 0 & 1 \\ Y_2 & 0 & 1 \\ \vdots & \vdots & \vdots \\ Y_n & 0 & 1 \end{bmatrix} \times \begin{bmatrix} \theta_c \\ \bar{Y}_c \\ \bar{X}_c \end{bmatrix} \quad (13)$$

where X_i and Y_i are the coordinates of the ith marker in the x-direction and y-direction, respectively. The relative motion of the geometric center can be estimated using the interstory drifts of the markers with the least square approach. As a result, the interstory drift of any location on the floor can be estimated if the relative motion of the geometric center and the coordinates of the location are known.

The floor of the building in this study was assumed to be a rigid body during an earthquake. In other words, we assumed that the interstory drift measured by the cameras due to in-plane rotation of the floor could be neglected in this study. Hence, it was assumed that the measured displacement between the cameras mounted on the ceiling and the markers on the floor was only contributed by the relative interstory drift.

2.2 Damage assessment

Fragility curves describe the probability of reaching or exceeding different states of damage given peak building response. Because IDR has been widely accepted as an indicator for building damage evaluation, the fragility curves of damage levels and IDR have been well-developed, and the US Federal Emergency Management Agency has adopted them in the nationally applicable standardized methodology for earthquake loss estimation (FEM, 2004). Naeim *et al*. (2006) applied fragility curves to assess the damage conditions of buildings instrumented with accelerometers under the Strong Motion Instrumentation Program of California, and the results were quite promising. In this study, we also employed fragility curves to evaluate post-earthquake damage levels using IDR values measured by the cameras.

As defined by FEMA, there are five structural damage levels, i.e., no damage, slight damage, moderate damage, extensive damage, and complete damage. The conditional probability of being in, or exceeding, a particular damage state, DS, given the IDR, δ, is defined by the following equation (FEMA 2004)

$$P(DS|\delta) = \Phi\left[\frac{1}{\beta_{DS}} ln\left(\frac{\delta}{\delta_{DS}}\right)\right] \tag{14}$$

where δ_{DS} and β_{DS} are the median and logarithmic standard deviation of the IDR at which the building reaches the threshold of the damage state DS, respectively, and Φ is the standard normal cumulative distribution function.

3. Experiment

A twin-tower steel building structure designed and constructed at the National Center for Research on Earthquake Engineering (NCREE) in Taiwan was used to experimentally test the proposed approach. As shown in Fig. 2, the structure consisted of a five-story tower on the right (denoted as Tower A) and a four-story tower on the left (denoted as Tower B). These two towers were coonected together using a plate at the first floor. The dimension of each story of the towers was 1.50 m wide × 1.10 m deep × 1.17 m high, and the mass of each floor was augmented with a 500-kg block. Each beam was made of A36 steel and had a U-shaped cross-section of 50 mm × 100 mm × 6 mm. Each column had a customized I-shaped cross-section with 100 mm × 5 mm web and 30 mm × 7 mm flanges. Because the structure was designed to collapse along the X-direction during the seismic excitation, the weak axis of the column was along the Y-direction. The sides of the towers along the Y-direction were installed with strong L-shaped braces, whereas those along the X-direction were installed with two types of tube braces. The outer diameters of these braces measured 18 mm and 21.7 mm, respectively, with thicknesses of 1.2 mm and 2 mm, respectively. By installing weaker tube braces in a specific story along the X-direction, the damage location was controlled. For the entire steel building, the beam–floor connections were welded, whereas the beam–column connections and the base–column connections were bolted.

Two cameras were installed on the ceiling of each floor, and a representative photograph is shown in Fig. 3. In total, 16 cameras were connected to a hub using an Ethernet connection, and each video signal was recorded at 30 fps by a network video recorder. The total cost of the hardware, including the 16 cameras, hub, and data acquisition system, was only 5,500 USD, which is much cheaper than the cost of other measurement systems. Eight targets were attached on each floor, as shown by the representative photograph in Fig. 4. In addition, two uniaxial accelerometers and two LVDTs were equipped at each floor and sampled at 200 Hz. The LVDT results were treated as the benchmark of the displacement measurements. Fig. 5 shows the locations of all the installed sensors including the cameras, LVDTs, and accelerometers.

The data recorded at the station TCU071 for the 1999 Chi-Chi earthquake record were exploited to excite the building in the X-direction. The peak ground acceleration of the first excitation was 200-gal, and this was increased to 1000-gal with intervals of 200-gal to induce gradually increased damage in the building. Three damage cases were

Fig. 2 The experimental twin-tower steel building

Fig. 3 The cameras installed on the ceiling at the second floor

Fig. 4 The eight markers on the first floor

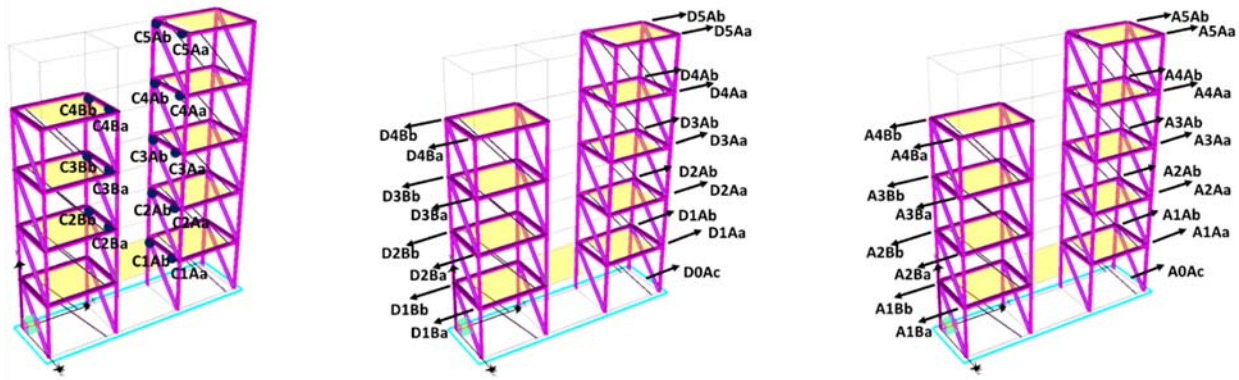

Fig. 5 The locations of the cameras (left), the LVDT (middle), and the accelerometers (right). There are four letters in each label of the sensors. In the first letter, "C", "D", and "A" represents the camera, LVDT, and accelerometer, respectively. In the second letter, the number represents the number of floors. In the third letter, "A" and "B" represents tower A and tower B, respectively. In the fourth letter, "a", "b" and "c" represents the inner side, outer side, and the middle, respectively

considered in the experiment. For Case 1, the weaker tube braces were located on the second story of Tower B; therefore, it was expected that the damaged story would be the second story of Tower B. For Case 2, it was expected that the damaged story would be the second story of Tower A, where the weaker tube braces were located for that case. For Case 3, the weaker tube braces were located on the first story of Tower A; therefore, it was expected that the damaged story would be the first story of Tower A.

Based on the category of the specimen that is a 5-story steel braced frame with high-code designed seismic level, the median and logarithmic standard deviation of the IDR of different damage states can be determined from the table provided by the HAZUS-MH technical manual(FEMA 2004). The median values of the IDR used in this specimen were 0.33%, 0.67%, 2.00%, and 5.33% for slight, moderate, extensive, and complete damage, respectively, whereas the logarithmic standard deviation values of the IDR were 0.124%, 0.124%, 0.126%, and 0.137% for slight, moderate, extensive, and complete damage, respectively. Hence, the fragility curves of the specimen could be drawn as shown in Fig. 6.

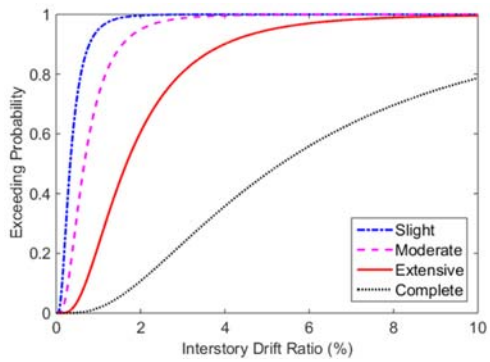

Fig. 6 The fragility curves of different damage states

4. Result

Because the interstory drifts at the stories with strong braces were always very small, in discussing the results of the interstory drift measurements, we focus, for the sake of conciseness, only on the stories with weak braces where both small and large interstory drifts were measured during the shaking. The time histories and amplitudes of the Fourier spectra of the interstory drift at marker M1 of the first story of Case 1 measured by the cameras, LVDTs, and accelerometers (ACC) are illustrated in Fig. 7. When the seismic excitation was 200-gal, the maximum interstory drift was less than 3 mm. Observing the time history measured by the cameras and LVDTs, it is evident that the amplitude measured by the cameras was much smaller than the one measured by the LVDTs. It seems that the used consumer-grade surveillance cameras were not sensitive to such small displacement. Therefore, the shape of the time history measured by the cameras was also quite different

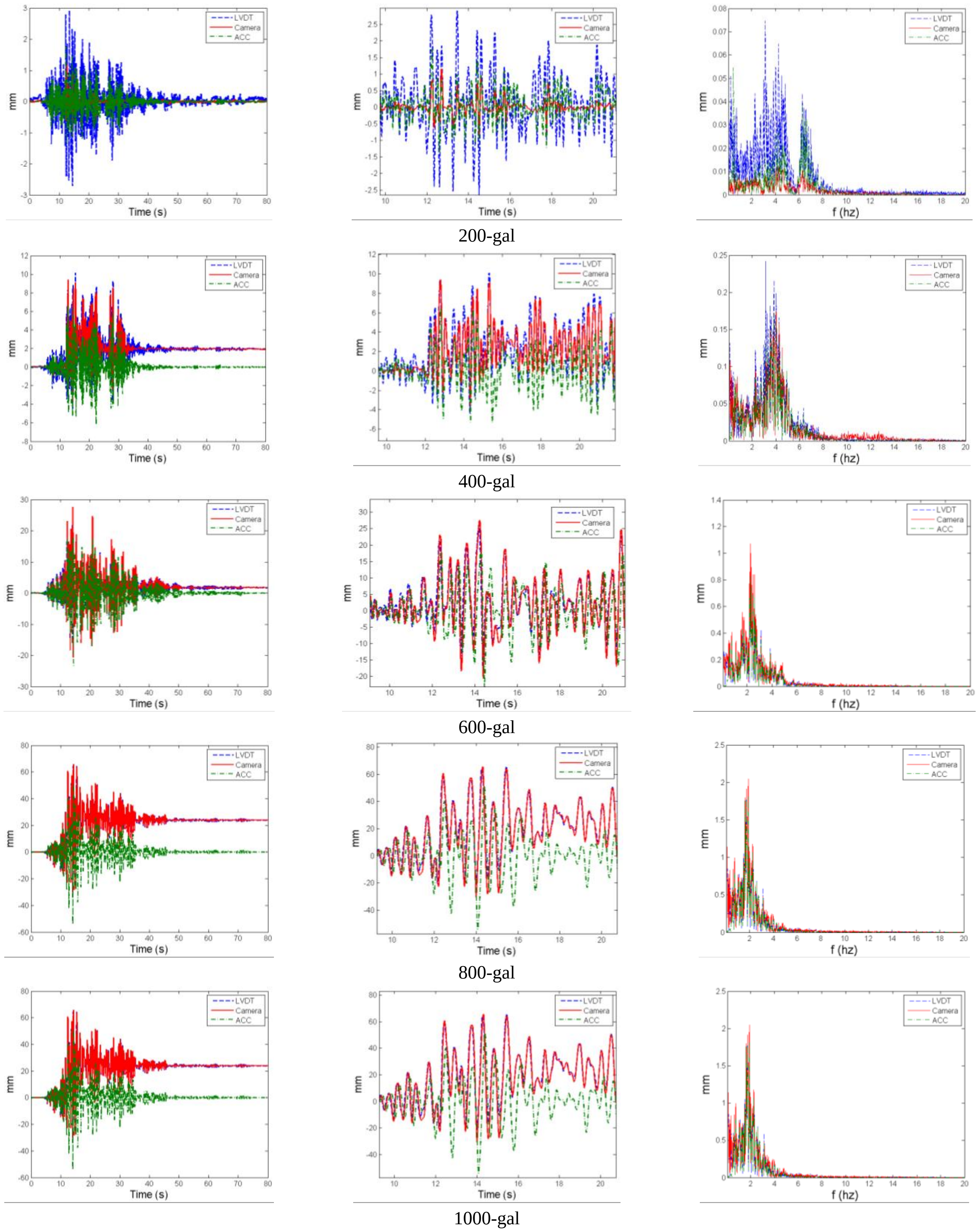

Fig. 7 The time history (left), close view of time history (middle) and Fourier spectrum (right) of the second story of Case 1 measured by the camera, LVDT, and accelerometer (ACC) under different seismic excitations

from the one measured by the LVDTs. The interstory drift can also be estimated using the acceleration measured at adjacent stories. The acceleration values at adjacent stories were integrated twice, and then a 0.075 Hz high-pass Butterworth filter was applied to remove the low-frequency drift after the numerical integration. Under such small deformation of the building, the time history of the interstory drift measured by the accelerometers was much closer to the one measured by the LVDTs, but the peak values values were still not so close. Furthermore, as observed from the Fourier spectra, most of the frequency content of the interstory drift was below 8 Hz. Unlike a high sampling rate, e.g., 200 Hz, for the structural acceleration response, a 30-fps sampling rate for the cameras was quite sufficient to capture the time history of the interstory drift of the building under seismic excitation.

When the seismic excitation increased to 400-gal, the maximum interstory drift increased to approximately 10 mm. Note that at the end of the time history there was a permanent residual interstory drift of approximately 2 mm measured both by the cameras and LVDTs, but not the accelerometers. Under this moderate amplitude of interstory drift, the time history measured by the cameras was not identical to the one measured by the LVDTs, but it was quite close. In contrast, although the high-frequency content of the acceleration data was quite close to that measured by the LVDTs, the interstory drift measured by the accelerometers was underestimated due to the removal of the extremely low-frequency content using the high-pass filter when residual deformation existed. A similar phenomenon was observed when the seismic excitation was increased to 600-gal, and the phenomenon became worse

Table 1 The interstory drift of the second story of Case 1 measured by camera, LVDT, and accelerometer under different seismic excitations

PGA = 200 gal	Interstory drift (mm)				Interstory drift ratio (%)	
	Maximum	Error	Residual	Error	Maximum	Error
M1	1.14	-1.74	0.00	-0.25	0.10	-0.15
M2	1.68	-1.20	-0.03	-0.28	0.14	-0.10
M3	0.71	-2.17	0.00	-0.25	0.06	-0.19
M4	1.58	-1.30	0.00	-0.25	0.14	-0.11
$\bar{X}_R$	1.21	-1.67	0.00	-0.25	0.10	-0.14
Accelerometer	2.75	-0.13	0.00	-0.25	0.24	-0.01
LVDT	2.88	-	0.25	-	0.25	-
PGA = 400 gal	**Interstory drift (mm)**				**Interstory drift ratio (%)**	
	Maximum	Error	Residual	Error	Maximum	Error
M1	12.01	2.33	2.08	-0.06	1.03	0.20
M2	10.80	1.12	2.20	0.06	0.92	0.10
M3	9.78	0.10	1.75	-0.39	0.84	0.01
M4	9.06	-0.62	1.76	-0.38	0.77	-0.05
$\bar{X}_R$	9.79	0.11	1.90	-0.24	0.84	0.01
Accelerometer	6.52	-3.16	0.00	-2.14	0.56	-0.27
LVDT	9.68	-	2.14	-	0.83	-
PGA = 600 gal	**Interstory drift (mm)**				**Interstory drift ratio (%)**	
	Maximum	Error	Residual	Error	Maximum	Error
M1	34.77	8.62	1.58	-0.37	2.97	0.74
M2	31.86	5.71	1.07	-0.88	2.72	0.49
M3	29.26	3.11	2.05	0.10	2.50	0.27
M4	27.28	1.13	1.79	-0.16	2.33	0.10
$\bar{X}_R$	29.13	2.98	1.73	-0.22	2.49	0.25
Accelerometer	23.21	-2.94	0.00	-1.95	1.98	-0.25
LVDT	26.15	-	1.95	-	2.24	-
PGA = 800 gal	**Interstory drift (mm)**				**Interstory drift ratio (%)**	
	Maximum	Error	Residual	Error	Maximum	Error
M1	79.96	13.52	25.01	1.65	6.83	1.16
M2	72.65	6.21	24.27	0.91	6.21	0.53
M3	68.48	2.04	24.05	0.69	5.85	0.17
M4	65.80	-0.64	24.17	0.81	5.62	-0.05
$\bar{X}_R$	68.52	2.08	23.27	-0.09	5.86	0.18
Accelerometer	53.91	-12.53	0.00	-23.36	4.61	-1.07
LVDT	66.44	-	23.36	-	5.68	-

Table 1 Continued

PGA = 800 gal	Interstory drift (mm)				Interstory drift ratio (%)	
	Maximum	Error	Residual	Error	Maximum	Error
M1	79.96	13.52	25.01	1.65	6.83	1.16
M2	72.65	6.21	24.27	0.91	6.21	0.53
M3	68.48	2.04	24.05	0.69	5.85	0.17
M4	65.80	-0.64	24.17	0.81	5.62	-0.05
$\bar{X}_R$	68.52	2.08	23.27	-0.09	5.86	0.18
Accelerometer	53.91	-12.53	0.00	-23.36	4.61	-1.07
LVDT	66.44	-	23.36	-	5.68	-
PGA = 1000 gal	Interstory drift (mm)				Interstory drift ratio (%)	
	Maximum	Error	Residual	Error	Maximum	Error
M1	108.58	7.45	51.62	1.33	9.28	0.64
M2	106.13	5.00	52.41	2.12	9.07	0.43
M3	104.99	3.86	51.44	1.15	8.97	0.33
M4	101.91	0.78	51.52	1.23	8.71	0.07
$\bar{X}_R$	104.08	2.95	51.72	1.43	8.90	0.25
Accelerometer	63.94	-37.19	0.00	-50.29	5.46	-3.18
LVDT	101.13	-	50.29	-	8.64	-

when the seismic excitation was increased to 800-gal and 1000-gal. Observing the results of the other cases indicated similar findings in those cases. Hence, figures for the other cases similar to Fig. 7 are not shown in this paper for the sake of conciseness.

The maximum interstory drift measured by the surveillance cameras using the proposed approach was compared to those measured by the accelerometers and the LVDTs. Table 1 summarizes the results of the different seismic excitations of Case 1 as a typical example. Note that only the results for one side, i.e., markers M1 trough M4, were considered for the first story in Case 1 because the image of the markers on the other side was blocked by the buckled brace. The maximum and residual interstory drifts measured by the LVDTs was treated as the reference, and the errors between the maximum and residual interstory drifts measured by the cameras at different markers and those measured by the LVDTs are also listed in the same table. The interstory drift measured by the cameras was actually between the location of the cameras on the ceiling and the location of the markers on the floor, and the location of the LVDTs was actually between markers M3 and M4.

Note that the interstory drifts measured at each marker should be almost identical if there is no torsional motion but, rather, only translational motion between the floors. However, with the exception of the results for when the seismic excitation was 200-gal, the maximum interstory drifts measured at the markers farther from the mass center were always larger. This implies that the damage to the braces when the seismic excitation was larger than 200-gal may have induced slightly torsional behavior of the floors of Tower B.

Using Eq. (13), the interstory drift at the mass center of the floor can be estimated using the ones at the different markers, and then the interstory drift at the location of each LVDT, denoted as $\bar{X}_R$, can be estimated if the coordinates of the location of the LVDT are given. The maximum interstory drift of $\bar{X}_R$ is also listed in Table 1. Because the location of $\bar{X}_R$ is coincident with the location of the LVDT, we used $\bar{X}_R$ to estimate the damage states in order to represent the results measured by the cameras in the following paragraphs. The errors of each marker ranged from approximately -1.20 mm to -2.17 mm when the building was subjected to 200-gal seismic excitation, but they increased gradually when the building was subjected to larger seismic excitations, with a maximum error of 13.52 mm at marker M1, which was the marker farthest from the mass center. This large error was due to the torsional effect and the fact that the locations of the LVDTs and the markers were actually different. However, the error of interstory drift of $\bar{X}_R$ remained less than 3 mm even when the building was subjected to larger seismic excitations. Such consistently small error results indicated that the accuracy of the interstory drift measured by the cameras was quite promising whether the building was subjected to small or large seismic excitations.

On the other hand, the interstory drift measured by the accelerometers was quite accurate when the building was subjected to 200-gal seismic excitation, with an error of only -0.13 mm, as listed in Table 1. However, when the building was subjected to 400-gal seismic excitation, with the residual interstory drift being increased to 2.14 mm, the error measured by the accelerometers was also increased because there was no permanent interstory drift measured by the accelerometers. The error was -3.16 mm when the building was subjected to 400-gal seismic excitation, and increased to -37.19 mm when the building was subjected to 1000-gal seismic excitation. Such large underestimations of IDR could very likely result in underestimations of damage levels.

Using the maximum IDR, the possibility of a given damage level can be estimated based on the fragility curves of different damage levels and IDRs, as described in Section 3. As listed in Table 1, when the building was subjected to 200-gal seismic excitation, all the IDR values measured by the cameras, accelerometers, and LVDTs were smaller than 0.33%, the median value of slight damage; hence, the damage state of no damage was estimated as the most probable for all the three measurements. When the building was subjected to 400-gal seismic excitation, all the IDR values were larger than 0.67%, the median value of moderate damage, except for the 0.56% IDR measured by the accelerometers. As a result, the damage state of moderate damage was estimated as the most probable damage state using the cameras and LVDTs, while slight damage was estimated as most likely using the accelerometers. When the building was subjected to 600-gal seismic excitation, all the IDR values were larger than 2.00%, the median value of extensive damage, except for the 1.98% IDR measured by the accelerometers. Fortunately, however, the damage state of extensive damage was still estimated as the most probable damage state by all three approaches. When the building was subjected to 800-gal seismic excitation, all the IDR values were larger than 5.33%, the median value of complete damage, except for the 4.61% IDR measured by the accelerometers. As a result, the damage state of complete damage was estimated as the most probable damage state using the camera and LVDTs, while extensive damage was estimated as most likely using the accelerometers. When the building was subjected to 1000-gal seismic excitation, the damage state of complete damage was estimated as the most probable damage state for all the three approaches because their IDR values were all larger than 5.33%.

The above discussion focuses only on the results for the first story in Case 1. Following the same procedure, damage estimation was conducted for all the other stories in Case 1, as summarized in Fig. 8. It is evident that the damage states estimated using the camera approach were identical to the ones estimated using the LVDT approach for all the stories at the different levels of seismic excitation, except with respect to the second story of Tower A under 800-gal excitation. The damage state was overestimated by one level using the proposed camera approach at that story. It is because there are always some errors in the measurement. When the maximum interstory drift measured by the camera is larger than the one measured by the LVDT, the damage state could be overestimated even when the maximum interstory drift measured by the camera merely exceeds the threshold of a certain damage state. On the other hand, although most of the damage states estimated using the accelerometer approach were identical to those estimated using the LVDT approach, the damage state for the second story of Tower B was underestimated by one level under both the 400-gal and 800-gal excitations mainly because the low-frequency drift was removed after the numerical integration, while that for the fifth story of Tower A was overestimated by one level under the 800-gal excitation probably due to the measurement error.

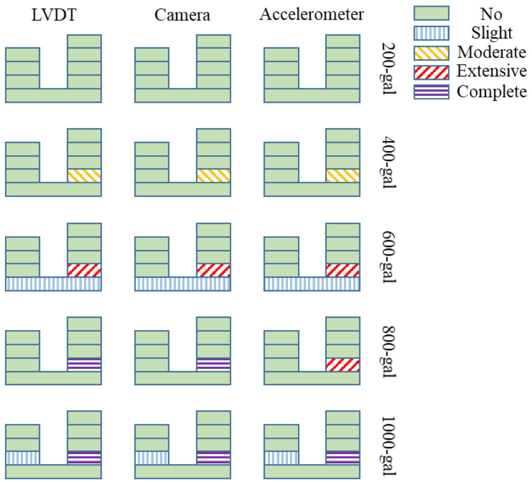

Fig. 9 Damage estimation results of all the stories of Case 2 under different seismic excitations

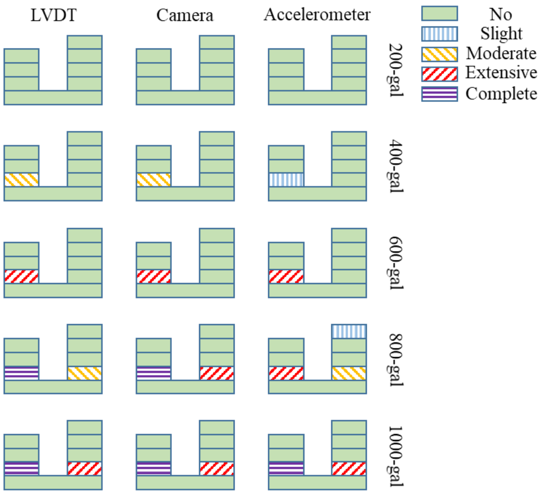

Fig. 8 Damage estimation results of all the stories of Case 1 under different seismic excitations

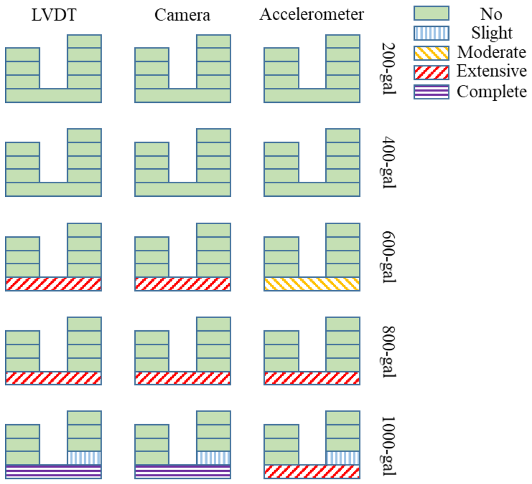

Fig. 10 Damage estimation results of all the stories of Case 3 under different seismic excitations

Table 2 The maximum interstory drift (mm) of the second story of Case 2 measured by camera, LVDT, and accelerometer under different seismic excitations

	PGA = 200 gal		PGA = 400 gal		PGA = 600 gal		PGA = 800 gal		PGA = 1000 gal	
Case 2	Maximum	Error	Maximum	Error	Maximum	Error	Maximum	Error	Maximum	Error
$\bar{X}_R$	3.49	-0.29	17.74	-1.16	43.58	-1.91	62.60	-2.29	187.70	-0.60
Accelerometer	2.73	-1.05	15.88	-3.02	41.50	-3.99	51.36	-13.53	80.30	-108.00
LVDT	3.78	-	18.90	-	45.49	-	64.89	-	188.30	-

Table 3 The maximum interstory drift (mm) of the first story of Case 3 measured by camera, LVDT, and accelerometer under different seismic excitations

	PGA = 200 gal		PGA = 400 gal		PGA = 600 gal		PGA = 800 gal		PGA = 1000 gal	
Case 2	Maximum	Error	Maximum	Error	Maximum	Error	Maximum	Error	Maximum	Error
$\bar{X}_R$	0.73	-0.41	2.24	-0.19	31.62	-1.10	57.67	0.45	223.68	-3.18
Accelerometer	1.26	0.12	2.66	0.23	18.64	-14.08	42.67	-14.55	58.18	-168.68
LVDT	1.14	-	2.43	-	32.72	-	57.22	-	226.86	-

Table 4 The RMSE of the interstory drift (mm) of the second story of Case 1, the second story of Case 2, and the first story of Case 3 measured by camera and accelerometer under different seismic excitations

PGA (gal)	Case 1		Case 2		Case 3	
	$\bar{X}_R$	Accelerometer	$\bar{X}_R$	Accelerometer	$\bar{X}_R$	Accelerometer
200	0.52	0.25	0.51	0.28	0.42	0.19
400	0.43	1.81	0.38	2.15	0.52	0.26
600	0.35	1.69	0.43	3.54	0.37	10.8
800	0.68	21.2	0.56	12.2	0.53	11.9
1000	0.71	45.3	0.62	9.02	0.82	135.1

Following the same procedure, damage estimation was also conducted for all the stories in Case 2 and Case 3, as summarized in Figs. 9 and 10, respectively. Observing these two figures, it is evident that all the damage states estimated using the camera approach were identical to the ones estimated using the LVDT approach. On the other hand, several damage states were underestimated using the accelerometer approach. These findings were similar to the ones for Case 1 mentioned above.

The maximum interstory drifts of Case 2 and Case 3 measured by the three approaches are also summarized in Tables 2 and 3, respectively. Unlike the results in Case 1 for 200-gal, when the interstory drift was small, i.e., for the 200-gal excitation in Case 2, the 200-gal excitation in Case 3, and the 400-gal excitation in Case 3, the accuracy of the interstory drift measured using the cameras was quite high. With the maximum interstory drift ranging from around 1.14 mm to 3.78 mm, the errors measured by the cameras were only around -0.41 mm to -0.29 mm, while the errors measured by the accelerometers were similar, around -1.05 mm to 0.23 mm. Again, however, when the maximum interstory drift was larger, the errors measured by the cameras were around -3.18 mm to 0.45 mm, while the errors measured by the accelerometers were quite large, even reaching as high as -168.68 mm. Besides the maximum interstory drift, the root-mean-square-error (RMSE) of the interstory drift measured by the camera and accelerometer under different seismic excitations are also calculated and summarized in Table 4. The RMSE is calculated using the interstory drift measured by the LVDT as reference. As can be observed in Table 4, while the values of RMSE of the camera retain quite small, the values of RMSE of the accelerometer increase dramatically when the magnitude of excitation increases because the low-frequency drift is removed after the numerical integration.

5. Conclusions

In this study, surveillance cameras were employed to evaluate post-earthquake building safety. A pair of surveillance cameras were installed on the ceiling of each story with several markers on the corresponding floor of the same story, which allowed the interstory drift of each story to be estimated using the images recorded during a seismic excitation. The fragility curves of the different damage levels and measured IDRs were used to estimate the possibility of different damage levels.

A series of steel building shaking table tests with incremental damage levels and IDRs were conducted to validate the performance of the proposed approach. Three types of sensors, i.e., LVDTs, cameras, and accelerometers, used to measure IDR values were compared. The results using IDRs calculated by LVDTs were treated as the reference ones. The results showed that when the interstory drift was less than 3 mm, the interstory drift as measured by the cameras tended to be underestimated because the cameras were not as sensitive to such small displacement as the LVDTs and accelerometers. Nonetheless, in observing the damage states estimated for all three damage cases using the cameras when the interstory drift was small, it was found that the results were all correct, i.e., no damage. When larger interstory drift occurred in the building, meanwhile, the interstory drift measured by the cameras seemed quite accurate, with maximum errors of approximately 3 mm for all the cases studied. The damage states estimated using the interstory drift as measured by the cameras were also quite accurate. However, when larger interstory drift occurred, the error measured by the accelerometers also increased in the underestimated direction due to their inability to measure permanent displacement. As a result, the damage states estimated using the accelerometers could very possibly be underestimated, mainly due to the low-frequency drift is removed after the numerical integration.

Note that in this study, it was assumed that the floor of the building was a rigid body during an earthquake. Further study is necessary, however, to consider the error of interstory measurement when the rotation at the location of the camera on the floor cannot be neglected. Nevertheless, this study shows the potential of the application of surveillance cameras for interstory drift measurements in buildings for post-earthquake safety assessments.

Acknowledgments

The authors are grateful to the financial support from the Ministry of Science and Technology of Republic of China under Grant MOST106-2622-M-011-002-CC2. This work was also financially supported by the Taiwan Building Technology Center from The Featured Areas Research Center Program within the framework of the Higher Education Sprout Project by the Ministry of Education in Taiwan.

References

Bouguet, J.Y. (2014), Camera Calibration Toolbox for Matlab. Software available at web address: http://www.vision.caltech.edu/bouguetj/calib_doc/

Bradski, G. and Kaehler, A. (2008), Learning OpenCV Computer Vision with the OpenCV Library, O'Reilly Media,WI, USA.

Federal Emergency Management Agency (2004), HAZUS-MH Technical Manual, Washington, D.C., USA.

Harvey Jr, P.S. and Elisha, G. (2018), "Vision-based vibration monitoring using existing cameras installed within a building", *Struct. Control Health Monit.*, **25**(11), e2235. https://doi.org/10.1002/stc.2235

Khuc, T. and Catbas, F.N. (2017), "Computer vision-based displacement and vibration monitoring without using physical target on structures", *Struct. Infrastruct. Eng.*, **13**, 505-516. https://doi.org/10.1080/15732479.2016.1164729

Lee, J., Lee, K.C., Cho, S. and Sim, S.H. (2017), "Computer vision-based structural displacement measurement robust to light-induced image degradation for in-service bridges", *Sensors*, **17**, 2317. https://doi.org/10.3390/s17102317

Naeim, F., Hagie, S., Alimoradi, A. and Miranda, E. (2006), "Automated post-earthquake damage assessment of instrumented buildings", In: *Advances in Earthquake Engineering for Urban Risk Reduction*, ed: Springer, pp. 117-134.

Park, J.W., Sim, S.H. and Jung, H.J. (2013), "Displacement estimation using multimetric data fusion", *IEEE/ASME Transact. Mechatron.*, **18**, 1675-1682. https://doi.org/10.1109/TMECH.2013.2275187

Skolnik, D.A. and Wallace, J.W. (2010), "Critical assessment of interstory drift measurements", *J. Struct. Eng.*, **136**, 1574-1584. https://doi.org/10.1061/(ASCE)ST.1943-541X.0000255

Trapani, D., Maroni, A., Debiasi, E. and Zonta, D. (2015), "Uncertainty evaluation of after-earthquake damage detection strategy", *Proceedings of 2015 IEEE Workshop on Environmental, Energy, and Structural Monitoring Systems, EESMS 2015*, pp. 125-130.

Yang, Y.S., Huang, C.W. and Wu, C.L. (2012), "A simple image-based strain measurement method for measuring the strain fields in an RC-wall experiment", *Earthq. Eng. Struct. Dyn.*, **41**(1), 1-17. https://doi.org/10.1002/eqe.1111

Yang, Y.S., Yang, C.M. and Huang, C.W. (2015), "Thin crack observation in a reinforced concrete bridge pier test using image processing and analysis", *Adv. Eng. Software*, **83**, 99-108. https://doi.org/10.1016/j.advengsoft.2015.02.005

Yang, Y.S., Wu, C.L., Hsu, T.T.C., Yang, H.C. and Lu, H.J. (2018), "Image analysis method for crack distribution and width estimation for reinforced concrete structures", *Automat. Constr.*, **91**, 120-132. https://doi.org/10.1016/j.autcon.2018.03.012

Yazgan, U. and Dazio, A. (2012), "Post-earthquake damage assessment using residual displacements", *Earthq. Eng. Struct. Dyn.*, **41**, 1257-1276. https://doi.org/10.1002/eqe.1184

Yoon, H., Elanwar, H., Choi, H., Golparvar-Fard, M. and Spencer Jr, B.F. (2016), "Target-free approach for vision-based structural system identification using consumer-grade cameras", *Struct. Control Health Monitor.*, **23**, 1405-1416. https://doi.org/10.1002/stc.1850

HJ